

Enhanced magnetocaloric effect and magnetic phase diagrams of single-crystal GdCrO_3

Yinghao Zhu,¹ Pengfei Zhou,¹ Tao Li,² Junchao Xia,¹ Si Wu,¹ Ying Fu,¹ Kaitong Sun,¹ Qian Zhao,¹ Zhen Li,^{3,4} Zikang Tang,¹ Yinguo Xiao,^{5,*} Zhenqiang Chen,^{3,4,†} and Hai-Feng Li^{1,‡}

¹*Joint Key Laboratory of the Ministry of Education,
Institute of Applied Physics and Materials Engineering, University of Macau,
Avenida da Universidade, Taipa, Macao SAR 999078, China*

²*Neutron Scattering Technical Engineering Research Center, School of Mechanical Engineering,
Dongguan University of Technology, Dongguan 523808, China*

³*Guangdong Provincial Engineering Research Center of Crystal and Laser Technology, Guangzhou, Guangdong 510632, China*

⁴*Department of Optoelectronic Engineering, Jinan University, Guangzhou, Guangdong 510632, China*

⁵*School of Advanced Materials, Peking University,
Shenzhen Graduate School, Shenzhen 518055, China*

(Dated: April 3, 2024)

The crystalline structure, magnetism, and magnetocaloric effect of a GdCrO_3 single crystal grown with the laser-diode-heated floating-zone technique have been studied. The GdCrO_3 single crystal crystallizes into an orthorhombic structure with the space group $Pmn2_1$ at room temperature. Upon cooling, under a magnetic field of 0.1 T, it undergoes a magnetic phase transition at $T_{\text{N-Cr}} = 169.28(2)$ K with Cr^{3+} ions forming a canted antiferromagnetic (AFM) structure, accompanied by a weak ferromagnetism. Subsequently, a spin reorientation takes place at $T_{\text{SR}} = 5.18(2)$ K due to Gd^{3+} - Cr^{3+} magnetic couplings. Finally, the long-range AFM order of Gd^{3+} ions establishes at $T_{\text{N-Gd}} = 2.10(2)$ K. Taking into account the temperature-(in)dependent components of Cr^{3+} moments, we obtained an ideal model in describing the paramagnetic behavior of Gd^{3+} ions within 30–140 K. We observed a magnetic reversal (positive \rightarrow negative \rightarrow positive) at 50 Oe with a minimum centering around 162 K. In the studied temperature range of 1.8–300 K, there exists a strong competition between magnetic susceptibilities of Gd^{3+} and Cr^{3+} ions, leading to puzzling magnetic phenomena. We have built the magnetic-field-dependent phase diagrams of $T_{\text{N-Gd}}$, T_{SR} , and $T_{\text{N-Cr}}$, shedding light on the nature of the intriguing magnetism. Moreover, we calculated the magnetic entropy change and obtained a maximum value at 6 K and $\Delta\mu_0 H = 14$ T, i.e., $-\Delta S_M \approx 57.5$ J/kg.K. Among all RECrO_3 ($\text{RE} = 4f^n$ rare earths, $n = 7-14$) compounds, the single-crystal GdCrO_3 compound exhibits the highest magnetic entropy change, as well as an enhanced adiabatic temperature, casting a prominent magnetocaloric effect for potential application in magnetic refrigeration.

I. INTRODUCTION

The GdCrO_3 compound was initially synthesized in 1956 [1]. Its crystalline structure was proved to be orthorhombic with the space group $Pbnm$ and lattice constants $a = 5.312$ Å, $b = 5.514$ Å, and $c = 7.611$ Å [2]. Recently, the space group was determined as $Pna2_1$ [3]. Later, its infrared and electronic absorption spectra were studied [4]. Albeit that the GdCrO_3 single crystal grown with a flux method may contain $\sim 1\%$ impurity, it was proposed that below ~ 7 K, the ionic Cr^{3+} magnetic sublattice underwent a spin reorientation from the Γ_4 (G_x , A_y , F_z) to the Γ_2 (F_x , C_y , G_z) magnetic structure. This was driven by the formation of the Gd^{3+} magnetic sublattice and the Gd^{3+} - Cr^{3+} couplings [5, 6]. The behavior of negative magnetization with a minimum centering around 25 K was observed in a polycrystalline GdCrO_3 sample, which was ascribed to the interactions between paramagnetic (PM) Gd^{3+} moments and the canted Cr^{3+} antiferromagnetic (AFM) moments [7]. It was reported that the GdCrO_3 compound displayed an electric polarization of $0.7 \mu\text{C}/\text{m}^2$ at $E = 2.25$ kV/cm, appearing simultaneously with the formation of Cr^{3+} magnetic struc-

ture below $T_{\text{N-Cr}}$ [3, 8]. The distortion in the GdCrO_3 structure was proposed to be associated with the off-center displacement of Gd atoms together with octahedral rotations via displacement of oxygen ions [3, 9]. Magnetic refrigeration has risen to be a new civilian refrigeration technology [10, 11]. Beside the ferroelectric property, the GdCrO_3 compound has attracted much attention and been believed to be a promising magnetorefrigerator material due to its high effective magnetic entropy change [12–15].

In this paper, we have grown a GdCrO_3 single crystal using laser diodes with the floating-zone (FZ) technique. We characterized the crystalline structure with a room-temperature x-ray powder diffraction (XRPD) study and the magnetic properties with a physical property measurement system (PPMS DynaCool instrument, Quantum Design). Based on our measurements, we studied the magnetocaloric effect (MCE) and found that the GdCrO_3 single crystal investigated in this study displayed the highest magnetic entropy change among all RECrO_3 compounds ($\text{RE} = 4f^n$ rare earths, $n = 7-14$). Moreover, we have built the magnetic phase diagrams as a function of applied magnetic field around the magnetic phase transitions of Gd^{3+} and Cr^{3+} ions, shedding light

on a further understanding of the nature of the intriguing magnetism.

II. EXPERIMENTAL

Polycrystalline samples of GdCrO_3 compound were synthesized using the conventional solid-state reaction method [16–18]. Chemically stoichiometric raw materials of Gd_2O_3 (ALFA AESAR, 99.9%) and Cr_2O_3 (ALFA AESAR, 99.6%) were milled and mixed by a Vibratory Micro Mill (FRITSCH PULVERISETTE 0) with an addition of 5–10% Cr_2O_3 compound. The mixture was calcined twice at ambient air pressure: Once was at 1100 °C for 24 h, and the other at 1200 °C for 36 h. We grew GdCrO_3 single crystals with a laser diode FZ furnace (Model: LD-FZ-5-200W-VPO-PC-UM) [19–21].

We pulverized a small piece of the single crystal to check the phase purity and determine the room-temperature crystalline structure with XRPD employing copper $K_{\alpha 1}$ (1.54056 Å) and $K_{\alpha 2}$ (1.544390 Å) with a ratio of 2:1 as the radiation. The XRPD pattern was collected at $2\theta = 20\text{--}90^\circ$ with a step size of 0.02° . We used the software FULLPROF SUITE [22] to refine the collected XRPD data. We modeled the Bragg peak shape with a Pseudo-Voigt function and used a linear interpolation between automatically-selected data points to estimate background contribution. The refining parameters are scale factor, zero shift, background contribution, peak shape parameters, asymmetry, preferred orientation, lattice constants, and atomic positions.

The measurements of dc magnetization and specific heat were carried out on a PPMS DynaCool instrument using the vibrating sample magnetometry and the heat capacity options, respectively. The dc magnetization at an applied magnetic field of 500 Oe was measured with two modes at 1.8–300 K: One was after cooling with 0 Oe, i.e., zero-field cooling (ZFC), and the other at $\mu_0 H = 500$ Oe, i.e., field cooling (FC). To clearly show the effect of applied magnetic field on magnetic structures of the two magnetic ions Gd^{3+} and Cr^{3+} , ZFC magnetization measurements at different fields as a function of temperature in two ranges (1.8–8 K and 165–172 K) were performed. ZFC magnetization measurements from –14 to 14 T at different temperatures were carried out either in a mode of the magnetic hysteresis loop or as a function of increasing magnetic field. In order to gain the adiabatic temperature change, the specific heats at 1.8–300 K were measured at magnetic fields of 0.5, 1, 2, 3, 5, 6, 8, 10, 12, and 14 T.

III. RESULTS AND DISCUSSION

A. Structural study

To study the crystalline structure of our grown GdCrO_3 single crystal, we pulverized a small piece of the GdCrO_3 single crystal and carried out a XRPD experiment at room temperature. Figure 1(a) shows the collected and refined patterns. Within the present experimental accuracy, the data can be well indexed with space group $Pmnb$. The corresponding crystalline structure in one unit cell was exhibited in Fig. 1(b), and the refined structural information was listed in Table I. The low values of the goodness of refinement validate our FULLPROF refinements. Our refined room-temperature lattice constants of the pulverized GdCrO_3 single crystal are $a = 7.6041(3)$ Å, $b = 5.5255(2)$ Å, and $c = 5.3102(2)$ Å, consistent with previously-reported values from a study with the polycrystalline GdCrO_3 compound [7].

B. Magnetic phase transitions

Figure 2 shows the measured magnetization as a function of temperature. As shown in the left of Fig. 2(a), as temperature decreases from 300 to 1.8 K, there is a smooth increase in the magnetization with an anomaly appearing around $T_{\text{N-Cr}}$ [Fig. 2(d)]. At $T_{\text{N-Cr}}$, we observed a small sharp increase [Fig. 2(d)]. This is by far clearer in the inverse magnetic susceptibility χ^{-1} , as shown in the right of Fig. 2(a). The magnetization increases smoothly again until around 25 K. We observed a maximum at T_{SR} [Fig. 2(c)]. Upon further cooling, there exists a kink at $T_{\text{N-Gd}}$ [Fig. 2(c)]. These anomalies are attributed to magnetic phase transitions. The first anomaly is related to Cr^{3+} ions, and $T_{\text{N-Cr}} \approx 168.97$ K at 0.06 T; the second one is ascribed to the spin reorientation of Cr^{3+} ions due to the gradual formation of Gd^{3+} moments [6], and $T_{\text{SR}} \approx 6.74$ K at 0.02 T; taking into account the fact that the ordering of 4f magnetic Gd^{3+} ions requires much lower temperatures [23, 24], the third one thus corresponds to the formation of long-range ordered Gd^{3+} magnetic structure, and $T_{\text{N-Gd}} \approx 2.33$ K at 0.02 T. The inverse magnetic susceptibility χ^{-1} in a pure PM state observes well with the Curie-Weiss (CW) law

$$\chi^{-1}(T) = \frac{3k_B(T - \Theta_{\text{CW}})}{N_A \mu_{\text{eff}}^2}, \quad (1)$$

where $k_B = 1.38062 \times 10^{-23}$ J/K is the Boltzmann constant, Θ_{CW} is the PM CW temperature, $N_A = 6.022 \times 10^{23} \text{ mol}^{-1}$ is the Avogadro's constant, and $\mu_{\text{eff}} = g\mu_B \sqrt{J(J+1)}$ is the effective PM moment. We fit the magnetization in the temperature range of 200–300 K ($> T_{\text{N-Cr}} > T_{\text{N-Gd}}$) to Eq. 1 and extrapolated the fit down to $M(\Theta_{\text{CW}}) = 0$, as shown in the right of Fig. 2(a).

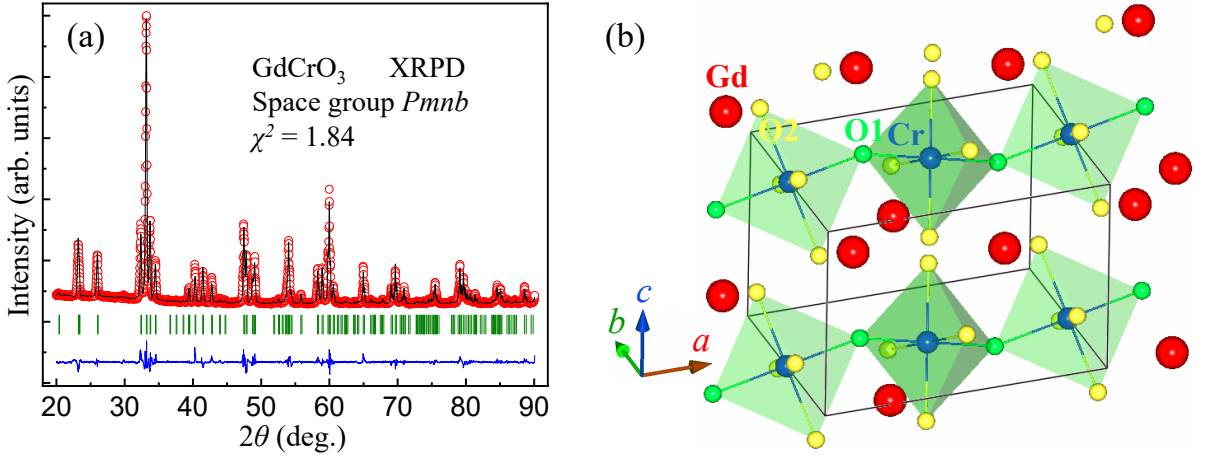


FIG. 1. (color online) (a) Observed (circles) and refined (solid line) XRPD patterns collected with a pulverized GdCrO_3 single crystal at room temperature. Vertical bars mark the positions of Bragg peaks. The bottom curve represents the difference between observed and refined XRPD patterns. (b) Crystal structure of GdCrO_3 compound in one unit cell (solid lines) with space group $Pmn\bar{b}$ (No. 62). The Gd, Cr, O1, and O2 ions were labeled.

TABLE I. Refined structural parameters, including lattice constants, unit-cell volume (V), atomic positions, and goodness of refinement, from room-temperature XRPD with a pulverized GdCrO_3 single crystal. The Wyckoff sites of all atoms were listed. We kept the atomic occupation factors (OCs) during FULLPROF refinements. The numbers in parentheses are the estimated standard deviations of the last significant digit.

XRPD with a pulverized GdCrO_3 single crystal (Orthorhombic, space group $Pmn\bar{b}$ (No. 62), $Z = 4$)					
a (Å)	b (Å)	c (Å)	V (Å ³)	$\alpha(=\beta=\gamma)$ (°)	
7.6041(3)	5.5255(2)	5.3102(2)	223.12(2)	90	
Atom	Site	x	y	z	OCs
Gd	4c	0.25	0.0588(2)	0.0151(3)	0.5
Cr	4b	0.00	0.00	0.50	0.5
O1	4c	0.25	0.4705(19)	0.1146(19)	0.5
O2	8d	0.0530(10)	0.2784(17)	-0.2935(16)	1.0
$R_p = 3.28$, $R_{wp} = 4.64$, $R_{exp} = 3.43$, and $\chi^2 = 1.84$					

This results in an effective PM moment $\mu_{\text{eff}} = 8.40(9) \mu_B$ and a PM CW temperature $\Theta_{\text{CW}} = -20.33(4)$ K. It is stressed that these values correlate with the PM behaviors of both Gd^{3+} and Cr^{3+} ions. Here, the extracted $\mu_{\text{eff}} = 8.40(9) \mu_B$ is a little larger than the previously-reported value $\sim 8.2 \mu_B$ from a study with the polycrystalline GdCrO_3 compound [25], indicating a better quality of the single-crystal GdCrO_3 sample. For Gd^{3+} ions (shell $4f^7$, quantum numbers $S = \frac{7}{2}$, $L = 0$, and $J = \frac{7}{2}$), the size of the theoretical (theo.) effective PM moment is $7.94 \mu_B$, while for Cr^{3+} ions, $\mu_{\text{eff,theo.}} = 3.873 \mu_B$ [26], therefore, $\mu_{\text{eff,theo.}} = \sqrt{7.94^2 + 3.873^2} \mu_B = 8.834 \mu_B$ for the GdCrO_3 compound. This theoretical value is $\sim 5.17\%$ larger than the corresponding experimental value $8.40(9) \mu_B$, which indicates that there exist probably vacancies in the Gd and/or Cr atomic sites. We calculated schematically the magnetic frustration parameter $f = \frac{|\Theta_{\text{CW}}|}{T_N}$ [21]; for Cr^{3+} ions at 0.05 T, $f_{\text{Cr}} \approx 0.12$. Compared with the

YCrO_3 compound within which the Y^{3+} ions are non-magnetic, and $f_{\text{Cr}} \approx 3.06$ [26], the competing degree of AFM and ferromagnetic interactions in GdCrO_3 compound is much weaker. The introduction of magnetic Gd^{3+} ions in GdCrO_3 compound has a strong effect on the magnetic structure of Cr^{3+} ions, in agreement with the appearance of T_{SR} .

To analyze individually the PM behavior of Gd^{3+} ions, we took the magnetization data in the temperature range of 30–140 K. This thermal range was within the interval ($T_{\text{N-Gd}}$, $T_{\text{N-Cr}}$) (Fig. 2), and far above $T_{\text{N-Gd}}$ (to ensure that Gd^{3+} ions were indeed in a PM state), and ~ 20 K below $T_{\text{N-Cr}}$ (to weaken the effect of ordered Cr^{3+} ions as much as possible). We first fit tentatively the data with

$$M = M_{\text{BG}} + \frac{m}{T - \Theta_{\text{CW}}}, \quad (2)$$

where M_{BG} is the contribution from background (BG) magnetization that includes actual BG magnetization

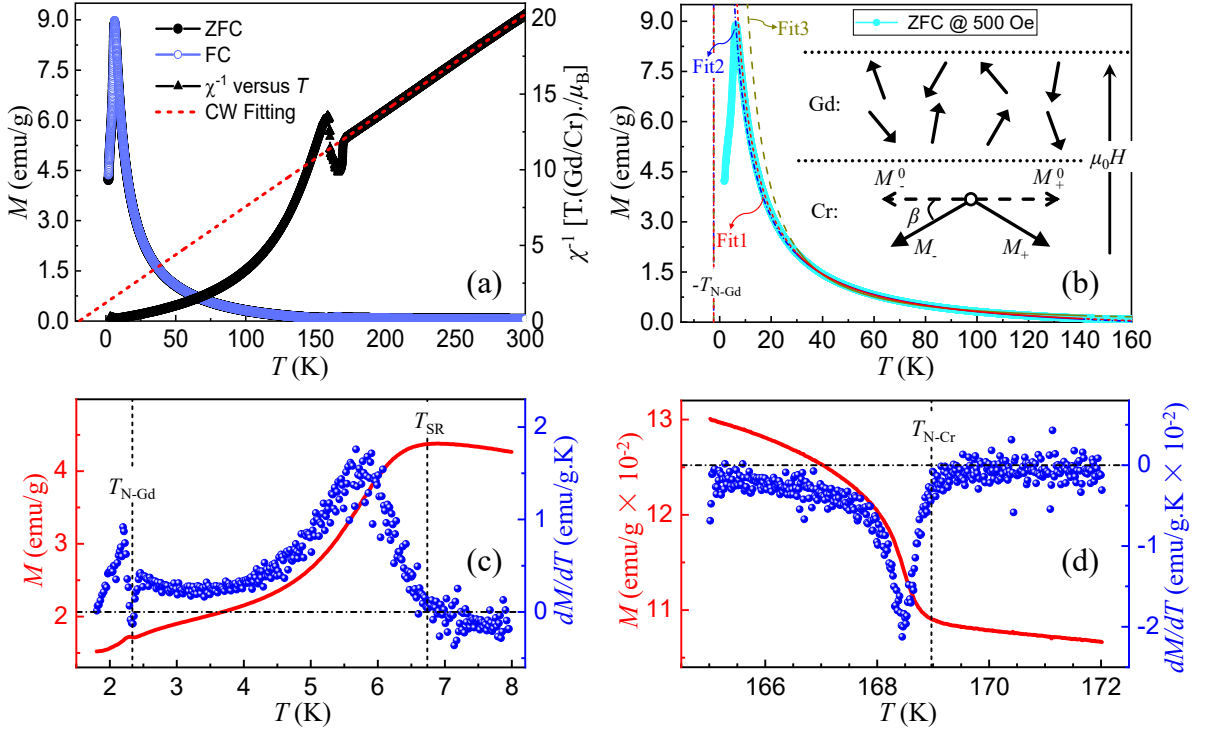


FIG. 2. (color online) Representative magnetization measurements of a small piece of GdCrO_3 single crystal with random crystallographic orientations. (a) ZFC (solid circles) and FC (void circles) magnetization (M) (left) and the corresponding ZFC inverse magnetic susceptibility (χ^{-1}) (solid up-angles) (right) at an applied magnetic field of 500 Oe as a function of temperature in the range of 1.8–300 K. The dashed line represents the fit with a CW law. (b) ZFC M versus temperature (solid circles) measured at 500 Oe from 1.8 to 160 K. The solid lines denote the fit1 (with Eq. 3), the fit2 (with Eq. 2), and the fit3 (with Eq. 3) in the temperature range of 30–140 K. They were extrapolated to the whole temperature regime [$-T_{\text{N-Gd}}$, 160 K] and shown as the short-dashed line (fit1), short-dash-dotted line (fit2), and the dashed-line (fit3). The inset schematically shows spin configurations of Gd^{3+} and Cr^{3+} ions within 30–140 K. See details in the text. (c) ZFC M (left), as well as the corresponding dM/dT (right), versus temperature in the range of 1.8–8 K at 200 Oe. $T_{\text{N-Gd}}$ points out the magnetic transition temperature of Gd^{3+} ions, which we define as the temperature point where the slope of $M-T$ curve is minimum. T_{SR} indicates the spin reorientation (SR) temperature of Cr^{3+} ions, which we define as the temperature point from which the slope of $M-T$ curve changes from negative to positive upon cooling. (d) ZFC M (left) and its slope ($=dM/dT$) (right) versus temperature in the range of 165–172 K at an applied magnetic field of 600 Oe. $T_{\text{N-Cr}}$ implies the magnetic transition temperature of Cr^{3+} ions, which we define as the temperature point at which a kink appears in the slope of $M-T$ curve upon cooling.

TABLE II. Fit values of the parameters M_{BG} and γ while modelling the temperature-dependent ZFC magnetization data of the GdCrO_3 single crystal (measured at 7–30 K and 500 Oe) with Eq. 3. We divided the whole temperature range into five regimes as listed below (see details in the text). During the refinements, we fixed $m = 114.17(51)$ emu.K./g and $\Theta_{\text{CW}} = -2.33$ K. The numbers in parentheses are the estimated standard deviations of the last significant digit.

T regime (K)	7–10	10–15	15–20	20–25	25–30
M_{BG} (emu/g)	1.312(12)	0.050(8)	-0.239(10)	-0.306(12)	-0.329(15)
γ	1.229(1)	1.144(1)	1.122(1)	1.115(1)	1.112(2)

from instrument, sample holder, as well as the glue, the temperature-independent diamagnetism components of Gd^{3+} and Cr^{3+} ions, the temperature-independent net magnetization of Cr^{3+} magnetic sublattice, and m is a constant. Similar modeling strategies were used previously [6, 7, 12, 27, 28]. The values of the diamagnetism of Gd^{3+} and Cr^{3+} ions are $\sim -2.0 \times 10^{-5}$ and $\sim -1.1 \times 10^{-5}$ emu/mol [29], respectively, which could be neglected rea-

sonably. Since the Gd^{3+} magnetic sublattice seems to form a long-range AFM order below $T_{\text{N-Gd}}$, most probably, the frustration parameter of Gd^{3+} ions $f = \frac{|\Theta_{\text{CW}}^{\text{Gd}}|}{T_{\text{N}}^{\text{Gd}}} \approx 1$, from which we deduced $\Theta_{\text{CW}}^{\text{Gd}} \approx -T_{\text{N}}^{\text{Gd}} \sim -2.33$ K. By forcing $\Theta_{\text{CW}}^{\text{Gd}} = -2.33$ K, we refined the data with Eq. 2 and obtained $M_{\text{BG}} = -0.473(33)$ emu/g, and $m = 80.823(22)$ emu.K./g, and the resultant fit was shown as fit2 in Fig. 2(b). It is worth noting that in Eq. 2, the net

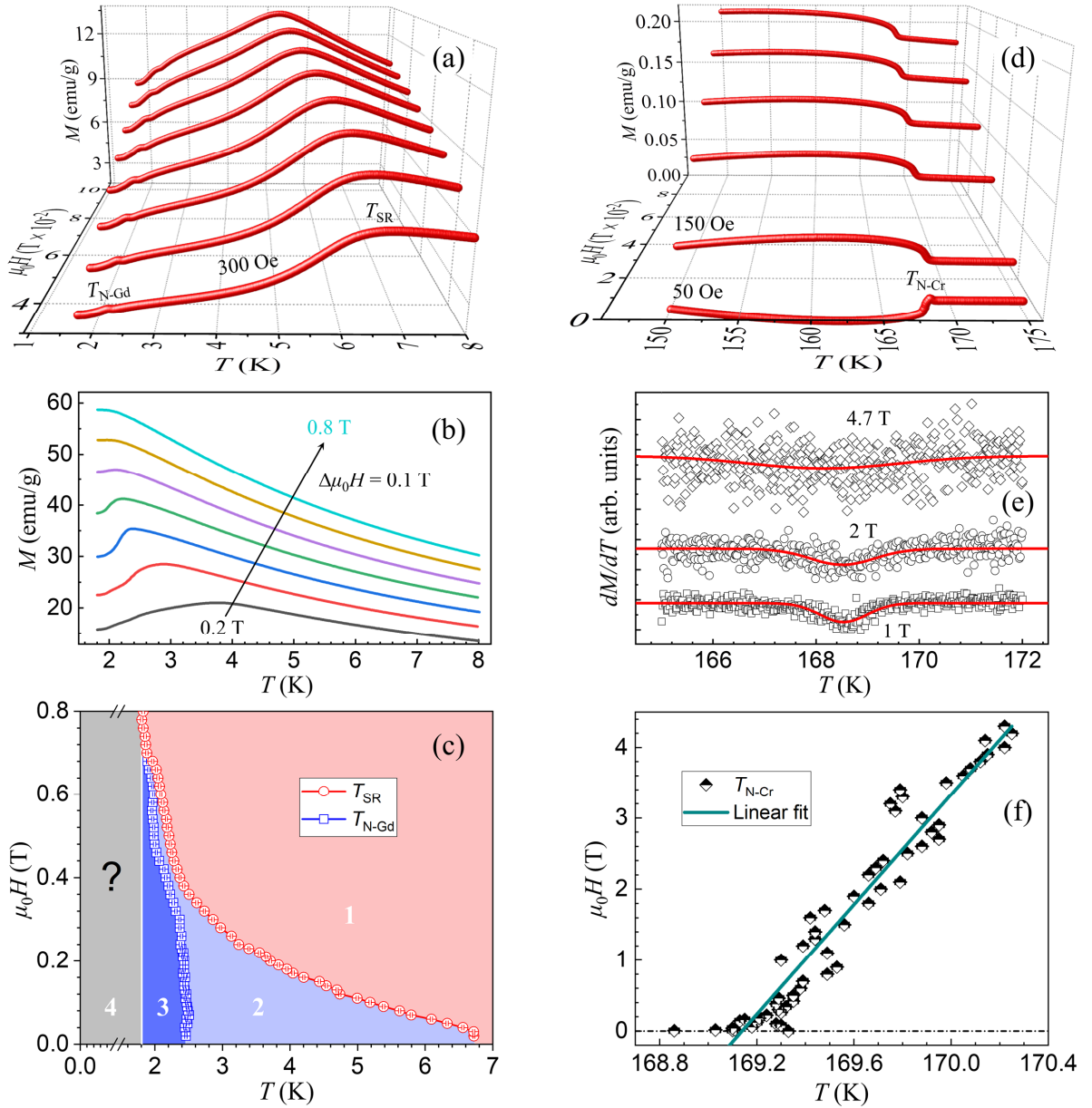


FIG. 3. (color online) ZFC M as a function of temperature from 1.8 to 8 K at applied magnetic fields of (a) 300–1000 Oe with a step size of 100 Oe, and (b) 0.2–0.8 T with $\Delta\mu_0 H = 0.1$ T. (c) Applied magnetic-field- and temperature-dependent phase diagram of T_{N-Gd} and T_{SR} . (d) ZFC M versus temperature from 150 to 175 K at applied magnetic fields of 50, 150, 400, 600, 800, and 1000 Oe. (e) Slope (dM/dT) (symbols) of $M - T$ curve at 1, 2, and 4.7 T. The solid lines are fits with a modified Gaussian function, as guides to the eye. (f) T_{N-Cr} as a function of applied magnetic field (symbols). We fit tentatively the data with a linear function (solid line).

magnetization of Cr^{3+} magnetic sublattice is supposed to be temperature independent, which is true only at low enough temperatures. For example, achieving this stage for the $YCrO_3$ single crystal, it requires temperatures at least below ~ 50 K [26].

For ferromagnets, it has been proved that the temperature-dependent magnetic susceptibility observes a power law $\chi_0^{-1} \propto (T - T_C)^\gamma$ at temperatures slightly above the Curie temperature T_C , where the exponential

parameter γ usually acts as a criterion for distinguishing the Heisenberg system ($\gamma = \frac{4}{3}$) from the Ising one ($\gamma = \frac{5}{4}$) [30, 31]. When $\gamma = 1$, it correlates with the CW model that is derived from the molecular-field theory; when $\gamma > 1$, it becomes a modified nonlinear formula that relates to the short-range spin correlations during the formation of the spin order [32, 33]. For antiferromagnets, there also exists a power-law model in describing the staggered magnetic susceptibility $\chi(Q) \propto \alpha(T - T_N)^{-\gamma}$ below T_N

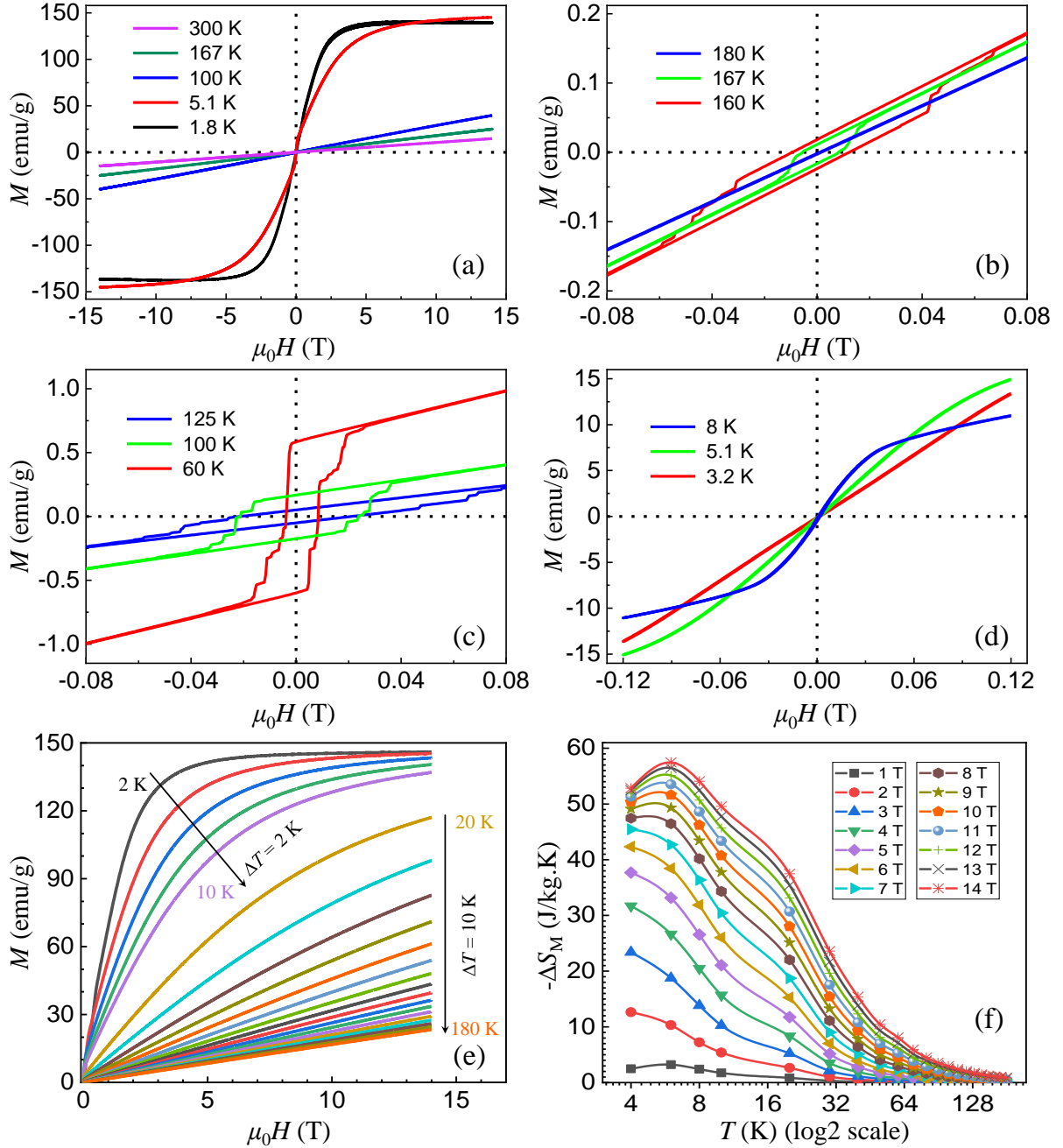


FIG. 4. (color online) (a-d) Representative ZFC isothermal magnetization versus applied magnetic field. (a) The field range is from -14 to 14 T, and the studied temperature points are at 1.8, 5.1, 100, 167, and 300 K. The measured temperature points are (b) 160, 167, and 180 K; (c) 60, 100, and 125 K; (d) 3.2, 5.1, and 8 K. For Figs. (b-d), the magnetic fields are from -1.2 to 1.2 T. (e) Representative ZFC magnetization as a function of applied magnetic field in the range of 0–14 T at temperatures of 2–10 K (step size 2 K) and 10–180 K (step size 10 K). (f) Extracted magnetic entropy versus temperature in the thermal range of 4–180 K (with log2 scale) at $\mu_0 H = 1$ –14 T with an interval of 1 T. The solid lines are guides to the eye.

[34]; when $\alpha = 1$, one may get the best fit [35].

Since T_{N-Gd} (2.33 K) \ll T_{N-Cr} (168.97 K), when the magnetic structure of Cr^{3+} ions establishes below T_{N-Cr} , the staggered magnetization could induce short-range Gd^{3+} magnetic orders due to possible Gd^{3+} - Cr^{3+} couplings [15, 36, 37]. To model these complicated magnetic

behaviors, we modified Eq. 2 into

$$M = M_{BG} + \frac{m}{(T - \Theta_{CW})^\gamma}, \quad (3)$$

where γ is a parameter representing both the short-range correlations of Gd^{3+} ions and the temperature-dependent component of net magnetization of Cr^{3+} magnetic sub-

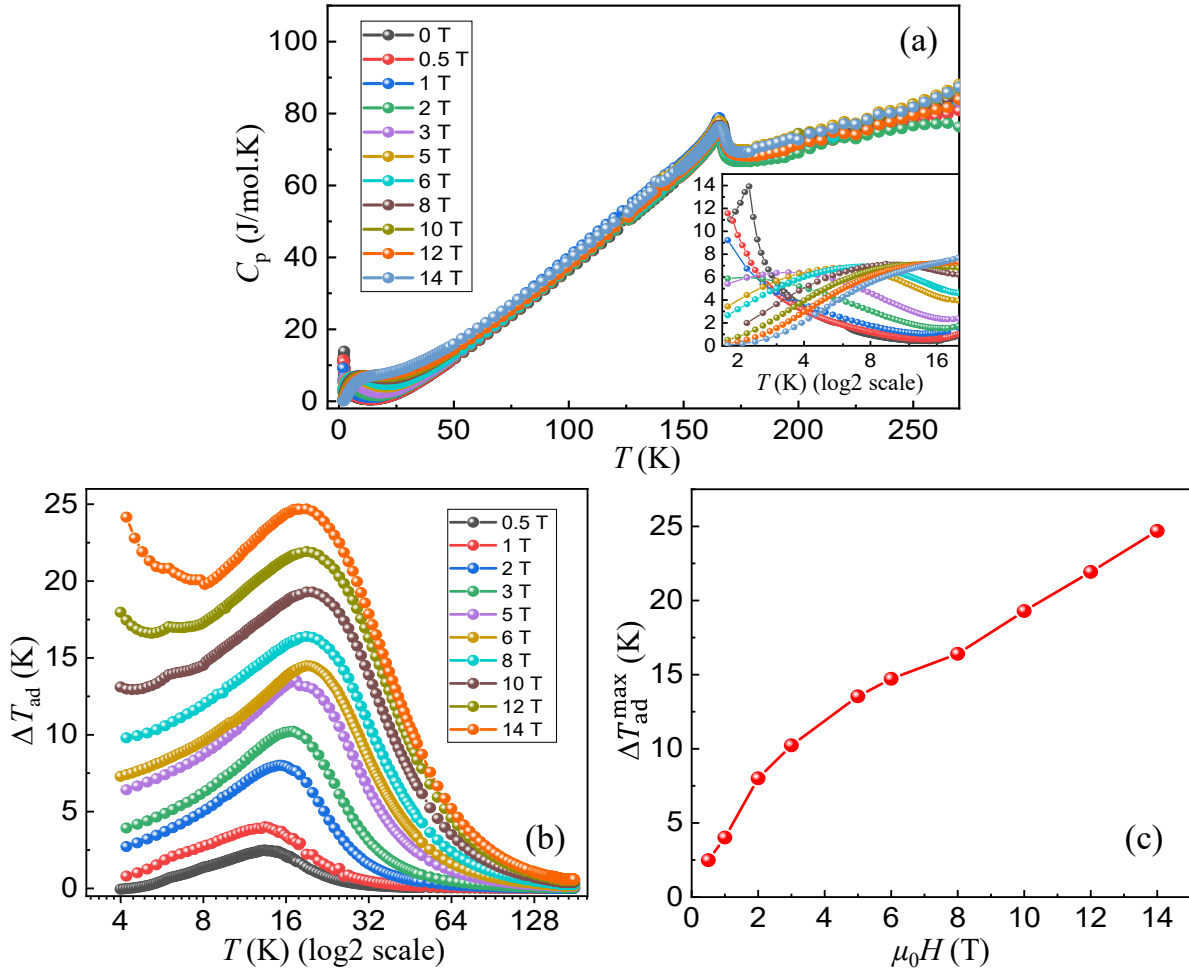


FIG. 5. (color online) (a) Temperature-dependent specific heat measured at applied magnetic fields of 0–14 T. Inset exhibits specific heats within the temperature range of 1.8–20 K with a log2 scale. (b) Temperature-dependent adiabatic temperature change (ΔT_{ad}) with applied magnetic fields from 0.5 to 14 T. (c) Maximum of adiabatic temperature change (ΔT_{ad}^{max}) versus applied magnetic field. In Figs. (a)–(c), the solid lines are guides to the eye.

lattice. This could be enhanced by the formation of magnetic polarons due to Gd^{3+} - Cr^{3+} ionic couplings [38, 39]. We took the following strategies for refinements in the thermal range of 30–140 K: (1) First, we kept $M_{BG} = 0$ and refined m and γ , which resulted in $m = 618.1(12)$ emu.K./g, and $\gamma = 1.6219(5)$, and the fitting result was shown as fit3 in Fig. 2(b). (2) While releasing M_{BG} , m , and γ , we refined them simultaneously, leading to $M_{BG} = -0.359(22)$ emu/g, $m = 114.17(51)$ emu.K./g, and $\gamma = 1.108(1)$, the best fit1 as displayed in Fig. 2(b). This best refinement is supported by the following facts (a) $T = 30$ K is a little above the temperature point ~ 24.51 K at which a kink appears in the slope of the $M-T$ curve and from where ZFC M increases sharply upon cooling due to the formation of AFM Gd^{3+} sublattice moments. (b) While extrapolating these fits to the temperature range from -2.33 to 160 K [Fig. 2(b)], the calculated values of $M(T)$ [short-dash-dotted line (fit2) and dashed line (fit3)] are deviated too much from the measured data below 30

K and above 140 K. It is noted that for the best fit1, the refined M_{BG} is still negative, which is much smaller than the values of diamagnetism of Gd^{3+} and Cr^{3+} ions, and $\gamma > 1$. As shown in the inset of Fig. 2(b), one possible configuration of spin moments during 30–140 K is (i) The magnetic Gd^{3+} ions stay in a PM state, i.e., all spins are theoretically aligned randomly with potential short-range correlations induced possibly by the formation of the magnetic order of Cr^{3+} ions. (ii) The formed Cr^{3+} AFM sublattice moments (M_+ and M_-) are canted downward from their AFM axis $M_+^0 M_-^0$ with an angle of β so that the net Cr^{3+} and Gd^{3+} moments are in opposite directions, leading to a negative value of M_{BG} . It is pointed out that mere the applied magnetic field of 500 Oe itself is hard to make an AFM canting [40] and produce so large net negative magnetization from the Cr^{3+} magnetic sublattice, consistent with the formation of a canted AFM Cr^{3+} structure.

To gain an in-depth understanding of the two magnetic

TABLE III. Comparison of the MCE in different RECrO_3 compounds ($\text{RE} = 4f^n$ rare earths, $n = 7-14$). Here PC = polycrystal, SC = single crystal, FZM = floating-zone method, FLM = flux method, T = tesla, T = temperature, Ref = reference, and TS = this study.

Compound	$4f^n$	Form	$-\Delta S_M$ (J/kg.K)			$\Delta\mu_0 H$ (T)	T (K)	Ref
			From Refs	From TS	Improved			
LaCrO_3		PC	0.1699	3.75	2107%	5	~ 37.1	[41]
GdCrO_3	7	SC (FZM)		57.47		14	6	TS
GdCrO_3	7	SC (FLM)	29.5	35.52	20.4%	4	3	[12]
GdCrO_3	7	PC	41.24	49.96	21.1%	9	3.8	[14]
TbCrO_3	9	SC (FLM)	5.0	11.97	139.4%	2	~ 4.5	[42]
DyCrO_3	10	PC	10.85	28.70	164.5%	4	5	[43]
HoCrO_3	11	PC	7.2	18.72	160%	7	20	[44]
ErCrO_3	12	PC	10.7	22.88	113.8%	7	15	[45]
TmCrO_3	13	PC	4.6	16.6	260.8%	5	~ 13.4 K	[46]
YbCrO_3	14	PC	~ 1.91	18.23	854.5%	5	~ 12.33	[47]

transitions occurring at 2.33 and 6.74 K, we further fit the temperature-dependent (from 7 to 30 K) ZFC magnetization data using Eq. 3. The m value in Eq. 3 is determined by the CW constant. We therefore fixed the parameters of m and Θ_{CW} (Table II) and released only M_{BG} and γ for the fits. To explore the detailed temperature-dependent values of M_{BG} and γ , we divided the temperature range of 7–30 K into five regimes, i.e., 7–10, 10–15, 15–20, 20–25, and 25–30 K. The fit results were listed in Table II. It is noted that as temperature decreases from 30 to 7 K, the value of γ increases, consistent with the hypothesis that there exist short-ranged AFM orders of Gd^{3+} ions above $T_{\text{N-Gd}}$. It is more interesting that the value of M_{BG} changes from negative (15–30 K) to positive (7–15 K). This sign change most probably indicates that the AFM axis of Cr^{3+} ions rotates, consistent with the observed spin-reorientation transition.

C. Magnetic phase diagrams

Figure 3 shows the measurements of magnetization as a function of temperature at different applied magnetic fields. The values of $T_{\text{N-Gd}}$ and T_{SR} were determined with the methods as claimed in Fig. 2(c). The indications of $T_{\text{N-Gd}}$ and T_{SR} were clearly observed at 300–1000 Oe [Fig. 3(a)]. With increasing applied magnetic field, the values of $T_{\text{N-Gd}}$ and T_{SR} shift to lower and lower temperatures [Figs. 3(b) and 3(c)]. Temperature-dependent magnetization curves around T_{SR} were previously measured at 0, 50, 500, and 1000 Oe [6, 12]. Unfortunately, due to the presence of impurities [6, 12], the indication of the SR transition disappeared when the strength of applied magnetic field was stronger than 1000 Oe, and the kink indicative of the AFM transition of Gd^{3+} ions at ~ 2.3 K didn't appear [12]. By comparison, our study clearly

shows both features with the high-quality GdCrO_3 single crystals. This makes us confident to deeply explore the detailed magnetic phase diagram.

As shown in Fig. 3(c), above ~ 0.68 T, the value of $T_{\text{N-Gd}}$ combines with that of T_{SR} , and the indication of $T_{\text{N-Gd}}$ is indistinguishable; above ~ 0.8 T, the signature of T_{SR} disappears, indicating that there exist applied-magnetic-field driven magnetic phase transitions [40]. We therefore divided the magnetic phase diagram [Fig. 3(c)] into four regimes. Within the regime 1, the ions of magnetic Cr^{3+} form a long-range ordered AFM structure with a small canting [Fig. 2(b)]. With decreasing temperature and increasing applied magnetic field, the AFM easy axis $M_+^0 M_-^0$ of Cr^{3+} magnetic ions changes from one direction to another (regime 2), depending on the competing degree between anisotropic exchange and single-ion anisotropic energies of Cr^{3+} ions as previously predicated theoretically [40]. While further decreasing temperature, the long-range magnetic order of Gd^{3+} ions forms (regime 3). The regime 4 hasn't been yet explored owing to the technique limitation. The applied magnetic field shifts $T_{\text{N-Gd}}$ to lower temperatures, resembling the behavior of a normal antiferromagnet. It is abnormal that the applied magnetic field also suppresses the values of T_{SR} , which necessitates a further hot-neutron scattering study to solve this puzzle. It is pointed out that the magnetic phase diagram of applied magnetic field and temperature [Fig. 3(c)] has been compiled with the measurements of magnetization, which strongly depends on the relative magnetic contributions of Gd^{3+} and Cr^{3+} ions [7].

As shown in Fig. 3(d), at 50 Oe, the M – T curve behaviors like an antiferromagnet. Upon cooling, the magnetization increases obviously at $T_{\text{N-Cr}} = 168.86(2)$ K and reaches a maximum at 168.40(2) K, subsequently, decreases sharply and then becomes negative at 167.99(2)

K, followed by a smooth decrease until ~ 162 K. After that, the magnetization increases again and becomes positive at ~ 149.73 K. Similar magnetic reversal was also observed in TmCrO_3 [46, 48], $\text{EuCr}_{0.85}\text{Mn}_{0.15}\text{O}_3$ [28], and YbCrO_3 [49] compounds. By contrast, above 150 Oe, the values of the measured magnetization always keep positive [Figs. 3(d) and 3(e)], and the magnetization in the temperature range from ~ 140 K to $T_{\text{N-Cr}}$ becomes larger and larger with increasing applied magnetic field so that the kink indicative of the appearance of $T_{\text{N-Cr}}$ [Fig. 2(d)] gets weaker and weaker and finally disappears above ~ 4.3 T [Figs. 3(e) and 3(f)]. The kink may be buried into the higher magnetization signal induced by higher applied magnetic fields, or its disappearance indicates a meltable magnetic state. Utilizing the method claimed in Fig. 2(d), we determined the values of $T_{\text{N-Cr}}$ as a function of applied magnetic field, as shown in Fig. 3(f). The applied magnetic fields enhance the values of $T_{\text{N-Cr}}$, consistent with the hypothesis that below $T_{\text{N-Cr}}$ the magnetic Cr^{3+} ions order with a canted AFM structure.

Figure 4(a) shows the ZFC magnetization as a function of applied magnetic field from -14 to 14 T at marked temperatures. At 1.8 K, the magnetization increases almost linearly from 0 to ~ 2 T and then approaches towards a saturation magnetic state above ~ 4 T. At 5.1 K, the saturated magnetization at 14 T is $\sim 4\%$ higher than that at 1.8 K, consistent with the formation of Gd^{3+} magnetic structure below $T_{\text{N-Gd}}$. We transferred the unit of magnetization from emu/g into μ_{B} per chemical formula unit (GdCrO_3) and obtained that the values of the saturation moments under 14 T were $\sim 6.43 \mu_{\text{B}}$ (at 1.8 K) and $\sim 6.69 \mu_{\text{B}}$ (at 5.1 K). These values are a little smaller than the theoretical saturation moment of Gd^{3+} ions, i.e., $g_J J = 7 \mu_{\text{B}}$, consistent with the foregoing discussions that the Gd^{3+} ions in GdCrO_3 compound form a long-range magnetic order. To check possible magnetic hysteresis effect, we measured the magnetization from -1.2 to 1.2 T in detail as temperature decreases from 180 to 3.2 K [Figs. 4(b)-4(d)]. As shown in Fig. 4(b), no hysteresis loop was observed at 180 K. Upon cooling, it appears at 167 K (below $T_{\text{N-Cr}}$), consistent with the hypothesis that the Cr^{3+} ions in GdCrO_3 compound form a canted AFM structure. Upon further cooling down to 60 K [Fig. 4(c)], the magnetic hysteresis effect gets more and more obvious with enhanced remanent magnetization. As shown in Fig. 4(d), at 8 K, the hysteresis loop becomes very small, and the magnetization shows a nonlinear field dependence, a characteristic feature of ferromagnetism or a short-range AFM state [40, 50]. At 5.1 , 3.2 , and 1.8 K (below T_{SR}), the magnetic hysteresis loops are indistinguishable. This may indicate that the canting degree of Cr^{3+} magnetic sublattice becomes very small, or there exists a magnetic phase transition for Cr^{3+} ions from the canted to a collinear AFM structure.

D. Magnetocaloric effect

To study the MCE of our grown GdCrO_3 single crystals, we measured field-dependent magnetization from 0 to 14 T at marked temperatures as shown in Fig. 4(e). The magnetic entropy change $-\Delta S_{\text{M}}$ can be calculated by

$$|\Delta S_{\text{M}}(T, \mu_0 H)| = \mu_0 \sum_i \frac{M_{i+1} - M_i}{T_{i+1} - T_i} \Delta H_i, \quad (4)$$

where $|\Delta S_{\text{M}}|$ is the absolute value of the magnetic entropy change, μ_0 is the permeability of vacuum, M_{i+1} and M_i represent measured values of magnetization at temperatures of T_{i+1} and T_i , respectively, ΔH_i is the differential element of the applied magnetic field. Based on Eq. 4, we calculated the values of $-\Delta S_{\text{M}}$ of single-crystal GdCrO_3 compound, and the results were shown in Fig. 4(f). It is clear that below 9 T, the value of $-\Delta S_{\text{M}}$ reaches a maximum at ~ 4 K; above 9 T, the maximum point shifts to an elevated temperature ~ 6 K. For example, at 6 K and 14 T, $-\Delta S_{\text{M}} \approx 57.47$ J/kg.K, which decreases rapidly upon warming. With the field change of $\Delta \mu_0 H = 9$ T, we calculated the magnetic entropy change $-\Delta S_{\text{M}} = 49.11$ J/kg.K at 4 K for the single-crystal GdCrO_3 sample. This value is $\sim 19.1\%$ higher than the value 41.24 J/kg.K measured with a polycrystalline GdCrO_3 sample under the same conditions at 3.8 K [14]. We compared the magnetic entropy changes of GdCrO_3 single crystals grown with two different methods: One was the flux method, where $-\Delta S_{\text{M}} = 29.5$ J/kg.K with $\Delta \mu_0 H = 4$ T at 3 K [12]; the second one was the laser-diode-heated FZ technique from the present study where $-\Delta S_{\text{M}} \approx 35.52$ J/kg.K (extrapolated) with the same values of $\Delta \mu_0 H$ and temperature, improved approximately 20.4% . It is obvious that single-crystal GdCrO_3 compound synthesized by the FZ method [19–21] shows a much stronger MCE than the polycrystalline samples, and even much better than the GdCrO_3 single crystal grown by the flux method [12]. As listed in Table III, we further compared our results with those from other RECrO_3 compounds. For example, at 20 K and 7 T, we calculated $-\Delta S_{\text{M}} \approx 18.72$ J/kg.K for the GdCrO_3 single crystal. This is $\sim 160\%$ larger than that of HoCrO_3 compound, 7.2 J/kg.K [44]. We also compared our results with those from other studies on DyCrO_3 [43], ErCrO_3 [45], etc., as listed in Table III. This demonstrates that single-crystal GdCrO_3 compound with enhanced MCE is a promising material for potential application in magnetic refrigerator.

With our measured temperature-dependent specific-heat data at different applied magnetic fields as shown in Figure 5(a), the adiabatic temperature change (ΔT_{ad}) can be calculated according to [51, 52]

$$\Delta T_{\text{ad}} = \int_0^{\mu_0 H} \frac{T}{C_p(T, \mu_0 H)} \left(\frac{\partial M}{\partial T} \right) \mu_0 H d\mu_0 H. \quad (5)$$

We calculated the temperature dependence of ΔT_{ad} as well as the applied magnetic-field-dependent maximum $\Delta T_{\text{ad}}^{\text{max}}$, as shown in Figs. 5(b) and 5(c), respectively. Figure 5(b) shows an applied-magnetic-field driven enhancement of ΔT_{ad} when $\mu_0 H \geq 10$ T. The grown GdCrO₃ single crystal in this study holds large values of adiabatic temperature change, e.g., $\Delta T_{\text{ad}}^{\text{max}} \approx 16.40$ K at 8 T, and 24.69 K at 14 T. The $\Delta T_{\text{ad}}^{\text{max}}$ value of single-crystal GdCrO₃ compound is much larger than that of other Gd-based perovskites such as GdMnO₃ and GdAlO₃ [52]. It is also larger than that of some lanthanides-based oxides such as EuHo₂O₄ ($\Delta T_{\text{ad}}^{\text{max}} \approx 12.7$ K) and EuDy₂O₄ ($\Delta T_{\text{ad}}^{\text{max}} \approx 16$ K) [53].

IV. CONCLUSIONS

In summary, we have investigated the structural and magnetic properties of the GdCrO₃ single crystal. The collected XRPD pattern was well indexed with the space group *Pmn*b, from which we extracted the lattice constants and atomic positions. The magnetization data at 500 Oe from 200 to 300 K observes well with the CW law, which results in a PM CW temperature $\Theta_{\text{CW}} = -20.33(4)$ K and an effective PM moment $8.40(9) \mu_{\text{B}}$. Taking into account both the temperature-dependent and -independent net-magnetization of Cr³⁺ ions, we can fit well the magnetization data at 30–140 K. We clearly observed the indications of the formation of canted AFM structure of Cr³⁺ ions at $T_{\text{N-Cr}}$, the spin reorientation of Cr³⁺ moments at T_{SR} , and the formation of long-range ordered Gd³⁺ magnetic structure at $T_{\text{N-Gd}}$. We have constructed the magnetic phase diagrams of $T_{\text{N-Cr}}$, T_{SR} , and $T_{\text{N-Gd}}$ as a function of applied magnetic field and proposed magnetic configurations in the corresponding temperature regimes. The magnetic phase diagrams of $T_{\text{N-Gd}}$ and $T_{\text{N-Cr}}$ are well consistent with the corresponding magnetic structures, whereas, the magnetic phase diagram of T_{SR} seems to be abnormal. When $T_{\text{SR}} < T < T_{\text{N-Cr}}$, obvious magnetic hysteresis loops were observed. Below T_{SR} , the hysteresis loop becomes very weak, probably indicating a decrease in the canting degree of the Cr³⁺ magnetic structure or a phase transition from the canted to a collinear AFM structure. We calculated the magnetic entropy change $-\Delta S_{\text{M}}$. For example, $-\Delta S_{\text{M}} \approx 35.52$ J/kg.K at $\Delta \mu_0 H = 4$ T and 3 K, improved $\sim 20.4\%$ than that of the GdCrO₃ single crystal grown by the flux method [12]. We summarized the MCE of RECrO₃ compounds (RE = 4^{fⁿ} rare earths, $n = 7-14$) and found that our grown GdCrO₃ single crystal displayed the highest value of magnetic entropy change and an enhanced adiabatic temperature change. This indicates that the single-crystal GdCrO₃ compound is a potential candidate for magnetic cooling.

The natural Gd atom is a very strong neutron absorber. Therefore, uniquely determining the interest-

ing magnetic structures, as well as the magnetic phase-transition diagrams explored in this study, necessitates a single-crystal neutron-diffraction study with a hot neutron source.

Acknowledgments

T.L. acknowledges the National Natural Science Foundation of China (Grant No. 11604214), the Foundation of Department of Education of Guangdong Province (Grant No. 2018KTSCX223), and the Foundation of Department of Science and Technology of Guangdong Province (Grant No. 2020A1515010814). Z.L. and Z.Q.C. acknowledge the Key-Area Research and Development Program of Guangdong Province (2020B090922006) and the Key Project of Natural Science Foundation of China (61935010, 61735005). H.-F.L. acknowledges the University of Macau (Files No. SRG2016-00091-FST and No. MYRG2020-00278-IAPME), the Science and Technology Development Fund, Macao SAR (Files No. 063/2016/A2, No. 064/2016/A2, No. 028/2017/A1, and No. 0051/2019/AFJ), and the Guangdong-Hong Kong-Macao Joint Laboratory for Neutron Scattering Science and Technology.

* y.xiao@pku.edu.cn (Y. Xiao)

† tzqchen@jnu.edu.cn (Z.-Q. Chen)

‡ haifengli@um.edu.mo (H.-F. Li)

- [1] S. Geller and E. A. Wood, *Acta Cryst.* **9**, 563 (1956).
- [2] S. Geller, *Acta Cryst.* **10**, 243 (1957).
- [3] S. Mahana, U. Manju, P. Nandi, E. Welter, K. R. Priolkar, and D. Topwal, *Phys. Rev. B* **97**, 224107 (2018).
- [4] G. V. S. Rao, C. N. R. Rao, and J. R. Ferraro, **24**, 436 (1970).
- [5] B. M. Wanklyn, *J. Cryst. Growth* **5**, 323 (1969).
- [6] A. H. Cooke, D. M. Martin, and M. R. Wells, *J. Phys. C: Solid State Phys.* **7**, 3133 (1974).
- [7] K. Yoshii, *J. Solid State Chem.* **159**, 204 (2001).
- [8] B. Rajeswaran, D. I. Khomskii, A. K. Zvezdin, C. N. R. Rao, and A. Sundaresan, *Phys. Rev. B* **86**, 214409 (2012).
- [9] S. Mahana, B. Rakshit, R. Basu, S. Dhara, B. Joseph, U. Manju, S. D. Mahanti, and D. Topwal, *Phys. Rev. B* **96**, 104106 (2017).
- [10] Y. F. Chen, B. H. Teng, Y. G. Chen, M. J. Tu, D. X. Tang, *Cryog Enics* **1**, 49 (2001).
- [11] O. Sari and M. Balli, *Int. J. Refrig.* **37**, 8 (2014).
- [12] L. H. Yin, J. Yang, X. C. Kan, W. H. Song, J. M. Dai, and Y. P. Sun, *J. Appl. Phys.* **117**, 133901 (2015).
- [13] S. Yin and M. Jain, *J. Appl. Phys.* **120**, 043906 (2016).
- [14] S. Mahana, U. Manju, and D. Topwal, *J. Phys. D: Appl. Phys.* **51**, 305002 (2018).
- [15] B. B. Dash and S. Ravi, *Solid State Sci.* **83**, 192 (2018).
- [16] H.-F. Li, *Synthesis of CMR manganites and ordering phenomena in complex transition metal oxides* (Forschungszentrum Jülich GmbH, Jülich, 2008).
- [17] H.-F. Li, Y. Su, J. Persson, P. Meuffels, J. M. Walter, R. Skowronek, and Th. Brückel, *J. Phys.: Condens. Matter* **19**, 016003 (2007).

- [18] H.-F. Li, Y. Su, J. Persson, P. Meuffels, J. M. Walter, R. Skowronek, and Th. Brückel, *J. Phys.: Condens. Matter* **19**, 176226 (2007).
- [19] Y. H. Zhu, S. Wu, Z. K. Tang, and H.-F. Li, *A method of centimeter-sized single crystal growth of chromate compounds and related storage device*, China Patent, 201,911,281,088.8.
- [20] S. Wu, Y. Zhu, H. Gao, Y. Xiao, J. Xia, P. Zhou, D. Ouyang, Z. Li, Z. Chen, Z. Tang, and H.-F. Li, *ACS Omega* **5**, 16584 (2020).
- [21] Y. Zhu, S. Wu, B. Tu, S. Jin, A. Huq, J. Persson, H. Gao, D. Ouyang, Z. He, D.-X. Yao, Z. Tang, and H.-F. Li, *Phys. Rev. B* **101**, 014114 (2020).
- [22] J. Rodríguez-Carvajal, *Phys. B.: Condens. Matter* **192**, 55 (1993).
- [23] J. Jensen and A. R. Mackintosh, *Rare Earth Magnetism: Structures and Excitations* (Clarendon Press, Oxford, 1991).
- [24] Q. Zhang, W. Tian, H.-F. Li, J.-W. Kim, J. Yan, R. W. McCallum, T. A. Lograsso, J. L. Zarestky, S. L. Bud'ko, R. J. McQueeney, and D. Vaknin, *Phys. Rev. B* **88**, 174517 (2013).
- [25] K. Sardar, M. R. Lees, R. J. Kashtiban, J. Sloan, and R. I. Walton, *Chem. Mater.* **23**, 48 (2011).
- [26] Y. Zhu, Y. Fu, B. Tu, T. Li, J. Miao, Q. Zhao, S. Wu, J. Xia, P. Zhou, A. Huq, W. Schmidt, D. Ouyang, Z. Tang, Z. He, and H.-F. Li, *Phys. Rev. Mater.* accepted, 004400 (2020).
- [27] I. Fita, R. Puzniak, A. Wisniewski, and V. Markovich, *Phys. Rev. B* **100**, 144426 (2019).
- [28] S. Kumar, I. Coondoo, M. Vasundhara, V. S. Puli, and N. Panwar, *Physica B* **519**, 69 (2017).
- [29] A. B. Gordon and F. B. John, *J. Chem. Educ.* **85**, 532 (2008).
- [30] C. Domb and M. F. Sykes, *Proc. Roy. Soc. (London)* **A240**, 214 (1957).
- [31] C. Domb and M. F. Sykes, *J. Math. Phys.* **2**, 63 (1961).
- [32] J. E. Noakes and A. Arrott, *J. Phys. Appl.* **35**, 931 (1964).
- [33] J. S. Kouvel and M. E. Fisher, *Phys. Rev.* **136**, A1626 (1964).
- [34] T. Moriya, *Progr. Theor. Phys.* **28**, 371 (1962).
- [35] Y. Ishikawa, Y. Endoh, and S. Ikeda, *J. Phys. Soc. Jpn.* **35**, 1616 (1973).
- [36] A. Jaiswal, R. Das, K. Vivekanand, T. Maity, P. M. Abraham, S. Adyanthaya, and P. Poddar, *J. Appl. Phys.* **107**, 013942 (2010).
- [37] M. Tripathi, T. Chatterji, H. E. Fischer, R. Raghunathan, S. Majumder, R. J. Choudhary, and D. M. Phase, *Phys. Rev. B* **99**, 014422 (2019).
- [38] H. Li, Y. Xiao, B. Schmitz, J. Persson, W. Schmidt, P. Meuffels, G. Roth, and Th. Brückel, *Sci. Rep.* **2**, 750 (2012).
- [39] Y. Zhang, K. Deng, X. Zhang, M. Wang, Y. Wang, C. Liu, J.-W. Mei, S. Kumar, E. F. Schwier, K. Shimada, C. Chen, and B. Shen, *Phys. Rev. B* **101**, 205126 (2020).
- [40] H.-F. Li, *npj Comput. Mater.* **2**, 16032 (2016).
- [41] L. Fkhar, A. Mahmoud, F. Boschini, M. Hamedoun, A. Benyoussef, E.-K. Hlil, M. Ait Ali, and O. Mounkachi, *J. Supercond. Nov. Magn.* **33**, 1023 (2020).
- [42] L. H. Yin, J. Yang, P. Tong, X. Luo, C. B. Park, K. W. Shin, W. H. Song, J. M. Dai, K. H. Kim, X. B. Zhu, and Y. P. Sun, *J. Mater. Chem. C* **4**, 11198 (2016).
- [43] A. McDannald and M. Jain, *J. Appl. Phys.* **118**, 043904 (2015).
- [44] S. Yin, V. Sharma, A. McDannald, F. A. Reboredo, and M. Jain, *RSC Adv.* **6**, 9475 (2016).
- [45] J. Shi, S. Yin, M. S. Seehra, and M. Jain, *J. Appl. Phys.* **123**, 193901 (2018).
- [46] K. Yoshii, *Mater. Res. Bull.* **47**, 3243 (2012).
- [47] G. Oliveira, thesis “Local probing spinel and perovskite complex magnetic systems” (2017).
- [48] K. Yoshii and N. Ikeda, *J. Alloy Compd.* **804**, 364 (2019).
- [49] Y. Su, J. Zhang, Z. Feng, L. Li, B. Li, Y. Zhou, Z. Chen, and S. Cao, *J. Appl. Phys.* **108**, 013905 (2010).
- [50] H.-F. Li, A. Senyshyn, O. Fabelo, J. Persson, B. Hou, M. Boehm, K. Schmalzl, W. Schmidt, J.-P. Vassalli, P. Thakuria, X. Sun, L. Wang, G. Khazaradze, B. Schmitz, C. Zhang, G. Roth, J. G. Rocah, and A. Wildes, *J. Mater. Chem. C* **3**, 7658 (2015).
- [51] A. Rostamnejadi, M. Venkatesan, P. Kameli, H. Salamat, J. M. D. Coey, *J. Magn. Magn. Mater* **323**, 2214 (2011).
- [52] S. Mahana, U. Manju, and D. Topwal, *J. Phys. D: Appl. Phys.* **50**, 035002 (2017).
- [53] A. Midya, N. Khan, D. Bhoi, and P. Mandal, *Appl. Phys. Lett.* **101**, 132415 (2012).